Mechanics Research Communications. Year	Publication Office: Elsevier UK
Editor-in-Chief: A. Rosato New Jersey Institute of Technology, Newark, New Jersey, USA Anthony.Rosato@njit.edu	

Elevated temperature nanoscratch of Inconel 617 Superalloy

Sepehr Salari[1], Md Saifur Rahman[2], Ali Beheshti[1*], Andreas A. Polycaropou[2*]

[1] *Department of Mechanical Engineering, George Mason University, Fairfax, VA, 22030, USA*
[2] *J. Mike Walker '66 Department of Mechanical Engineering, Texas A&M University, College Station, TX, 77843, USA*
**Corresponding authors: abehesh@gmu.edu Tel.: + 1(703) 993-5638; and apolycarpou@tamu.edu Tel.: +1(979)458-5763*

Abstract

Inconel 617 superalloy is a main candidate to be used for mechanical and tribo-components in high temperature helium-cooled reactors. Recent findings show that it grows a unique surface oxide, especially under high temperature helium with distinct wear, friction, and contact properties. This study reports the elevated temperature nanoscratch behavior of Inconel 617 and further utilizes it to understand the effect of temperature on contact friction constituent contributors, adhesion and plowing at small scales. Inconel 617 is aged in high temperature helium, and consequently, the total kinetic friction coefficient of the alloy surface oxide is obtained in temperatures ranging from 25°C to 400 °C. A finite element model is developed and validated based on the experimental results. The model is then utilized along with previously established techniques to determine the adhesion and plowing components of the friction coefficient. At small scale, the experimental results show that with increasing temperature the friction coefficient increases. It was inferred that this increase is mainly due to the increased contribution of plowing friction at high levels of deformation.

[Graphical Abstract]

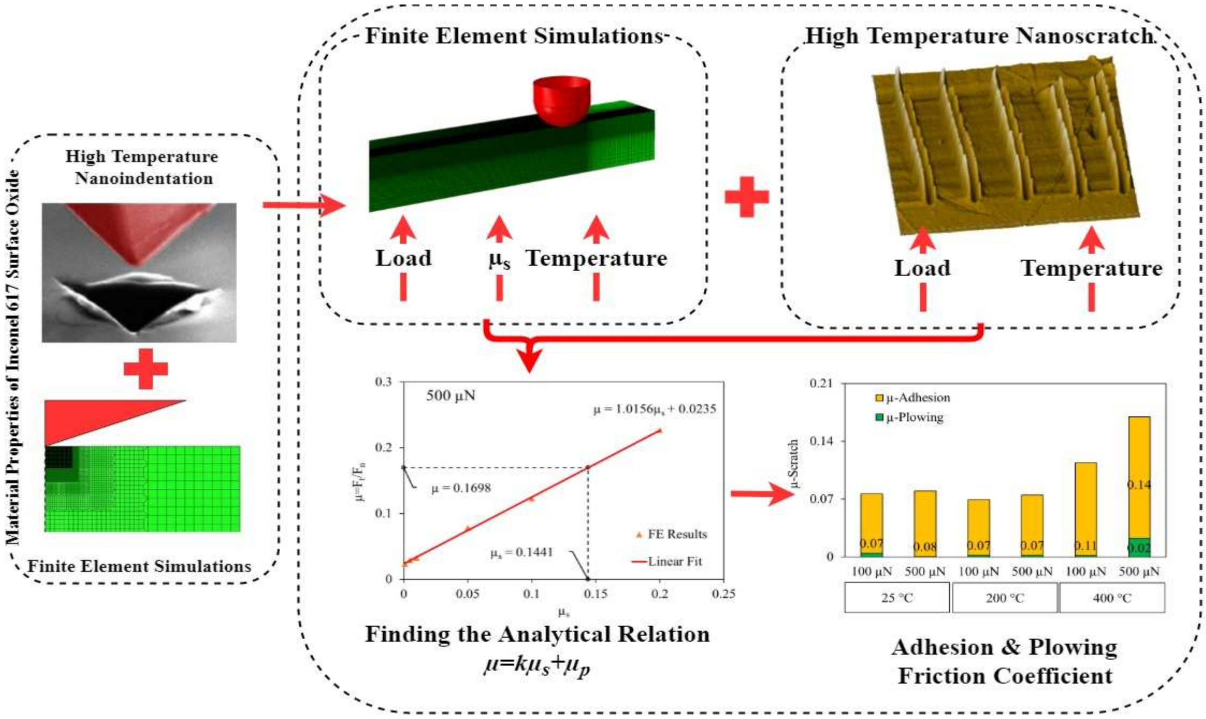

Keywords: Inconel 617, Nicke-based Superalloys, Scratch Friction, High Temperature, Adhesion, Plowing

1. Introduction

In view of design demands, materials that can withstand harsh environment and high temperature (HT) conditions are essential for reliable and efficient operation of mechanical components in applications such as jet engines, gas turbines, heat exchangers and cooling systems, among others. HT superalloys, with superior mechanical properties and surface stability, are among the primary solutions to overcome the challenges associated with these applications. In particular, polycrystalline nickel-based Inconel 617 superalloy (IN617) is one of the principal candidates for next-generation very-high-temperature reactors with outlet temperatures up to 950°C [1–3]. These reactors are mainly cooled by Helium (He) with low levels of impurities. Under these conditions, the metallic alloys can inevitably develop unique surface oxides that can impact the movement of the tribo-components and their contact interactions specifically at HT [4–6]. Furthermore, reactors tribological components (e.g., valves and control rods) are subjected to low-speed intermittent oscillatory motion often combined with long idle times. Accordingly, their contact and sliding behaviors are very important in maintaining reactor operational integrity and safety. While macro-HT wear, friction and self-welding of IN617 have been investigated [4–9] (including several works by the authors), a deeper understanding of the mechanics involved in the coefficient of friction (COF) behavior and its constituents (adhesion and plowing components) at smaller scale is highly beneficial, especially in view of the fact that IN617 develops micro-size surface oxides with different properties than its bulk.

Nano/micro-scratch is a useful method of measuring tribological performance, e.g., friction and wear properties [10–12], mechanical failure of thin films, and adhesion strength [13–16]. This technique can be complemented by finite element (FE) models to get more insight into the surface contact, deformation and friction behavior (see for example Refs. [17–21]). Among them, is the work of Subhash and Zhang who built a FE model to investigate the influence of interfacial COF, μ_s, and the attack angle of indenter on overall COF [17]. Further, the connection between the adhesion frictional component μ_a, the plowing friction component, μ_p and the overall COF ($\mu = \mu_a + \mu_p$) was analyzed [17]. This model was further improved to include Berkovich tip orientation and its influence on plowing and adhesion parts of the COF by Chamani and Ayatollahi [18]. In another related study, Chamani and Ayatollahi, used nanoscratch FE analysis to find material flow around the indenter and introduced a technique (called focal point method) to examine the adhesion part of the COF [19]. Notwithstanding its challenges, HT nanoscratch testing has recently gained interest due to its capability in understanding small scale tribological performance of advanced engineered alloys, coatings and microelectromechanical systems at elevated temperature applications [22–25]. However, consolidated experimental and FE analysis at HT, especially aiming at finding the plowing and adhesion components of the COF is lacking in the literature.

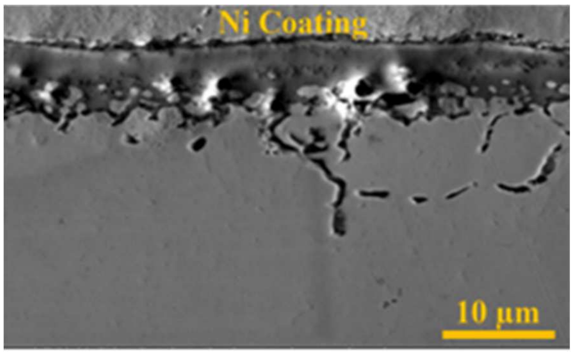

Fig. 1 Cross section SEM image of aged IN617 showing the bulk material and oxide layer (the Ni coating on top is to stabilize and protect the developed oxide), taken from [9].

The current study investigates nano/micro-scale frictional behavior of IN617 top surface oxide in temperatures ranging from 25 °C to 400 °C following the method developed by Subhash and Zhang and its adaptation by Chamani and Ayatollahi [17,19]. Nanoscratch technique and its associated normal/tangential load and displacement are used to study kinetic friction behavior of the alloy aged in He at 950 °C. In addition, kinetic friction, and its components (plowing and adhesion) evolution with temperature and load are investigated using FE analysis. The accuracy of the method is also validated with experimental results of multi-scratch tests.

2. Materials and Methods

2.1. Sample Preparation

IN617 samples were received from Idaho National Laboratory (INL), Idaho, USA. To simulate the effect of the He-cooled reactor environment, the samples were then placed in a 99.999%-pure He filled furnace at 950°C and aged for 100 hours (details on chemical composition of the as-received alloy as well as aging process can be found in Refs. [4,5]). **Fig. 1** shows the developed oxide layer over the bulk IN617 that varies in thickness from 6 to 10 µm. To compare the surface behavior of the bulk and the oxide and to facilitate FE analysis validation, two sets of samples were prepared, virgin (bulk) and aged IN617. The virgin IN617 samples were polished to have roughness values of 0.03 µm to 0.04 µm. After the preparation of the aged samples, their best roughness value that could be obtained through polishing was around 0.45 µm which was too high for the scratch tests. Accordingly, the nanoscratch experiments were performed on the cross section of the oxide of aged IN617 with approximate roughness of 0.04 µm. Detailed sample preparation can be found elsewhere [9].

2.2. Nanoscratch Experiments

Nanoscratch experiments were conducted using a commercial nanoindenter (Triboindenter TI Premier, Bruker Inc.). For room-temperature experiments, the nanoscratch tests were performed with constant normal loads in the range of 100 to 500 µN with a conospherical indenter of 5µm tip radius. In addition, higher loads of 1 to 5 mN, were used for the FE model

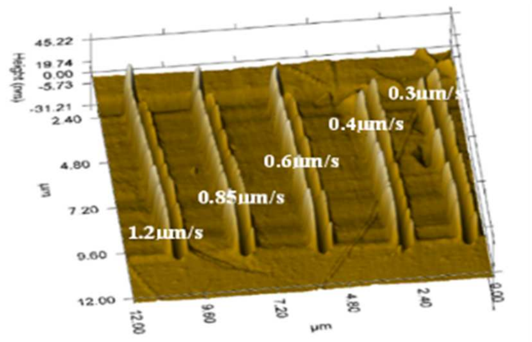

(a)

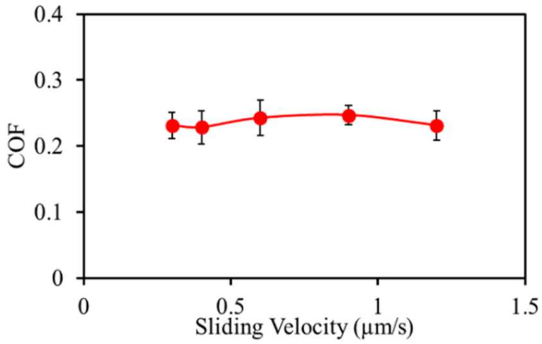

(b)

Fig. 2 a) Sample SPM image of residual scratches at different velocities and b) Variation of COF with sliding velocity at a normal load of 500 μN on polished virgin samples. Error bars show the standard deviation of measured COF for different tests and at each sliding velocity.

verification. Tests were performed in three steps of increasing the normal load to its maximum value (indentation) and, subsequently, scratch the surface while keeping the normal load constant, followed by the unloading step. The nanoscratch test completed at elevated temperatures was limited to only a lower normal load set due to excessive surface softening and penetration depth at higher loads. The nanoindenter is equipped with a transducer with very low drift. For the experiments, the overall drift rate including the thermal drift was recorded at less than 0.5 nm/s. Thermal drift rate was in the range of 0.1-0.3 nm/s with the maximum value occurring at 400 °C. Details on calibration and drift rate of the nanoindenter is provided in Ref. [9]. To protect the tip at HT, all the HT nanoscratch tests were performed under the cover of 95% Argon and 5% Hydrogen gas mixture. Nanoscratch tests were repeated at least 5 times at each temperature while the length of the scratch was kept constant at 10 μm. It should be added that the nanoscratch experiments were performed on the surface of virgin samples, however, due to high roughness of the oxide surface discussed above, the experiments were performed on the cross section of the aged samples.

The normal and friction forces, as well as the normal and lateral displacements were recorded for each scratch test. Using a low load of 2 μN, a trace and retrace scan were performed, before and after the scratch test to be able to perform tilt correction and calculate the residual depth due to the scratch.

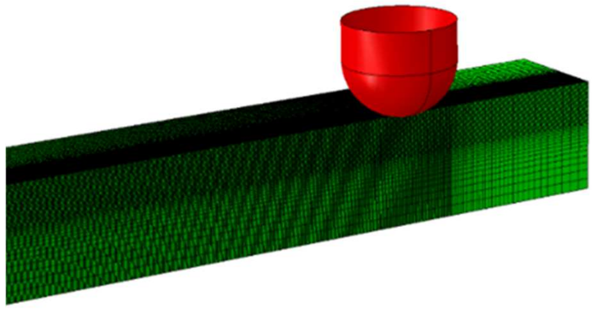

Fig. 3 FE model of the nanoscratch simulations.

The system also has a scanning probe microscopy (SPM) capability through which in-situ surface topography can be investigated using the same low contact force tracing. For high temperatures, the overall drift rate including the thermal drift was recorded and was kept less than 0.5 nm/s. In addition, the normal load of 500 μN was applied and repeated with varying sliding velocities in the range of 0.3 – 1.2 μm/s to find out if sliding velocity at this range has an effect on the results and especially frictional heating. **Fig. 2a** shows a typical SPM image of the residual scratches for different scratch rates. The variation of COF with varying sliding velocities is also depicted in **Fig. 2b** where no significant dependence on sliding velocity can be concluded. Nonetheless, it should be noted that the range of velocity used here is limited and as a result, independency of COF on sliding velocity cannot be generalized for velocities that are out of the current range.

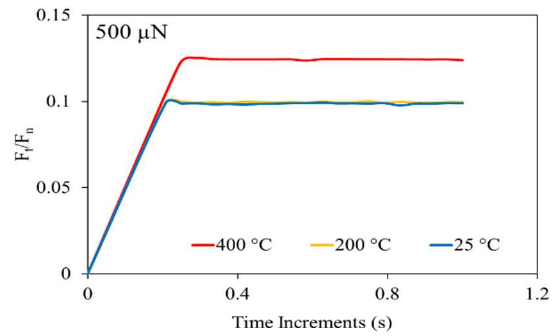

(a)

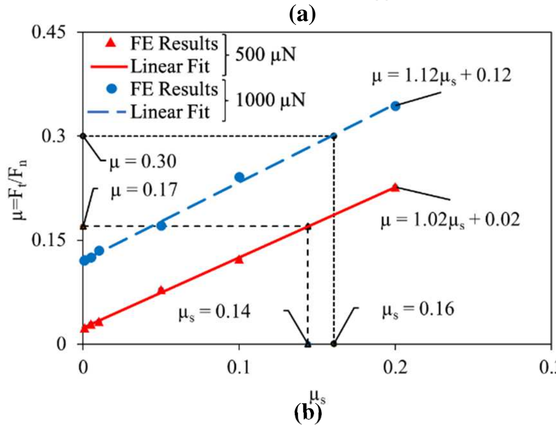

(b)

Fig. 4 a) Generated tangential load over normal load at sample normal load of 500 μN for each temperature and b) examples of linear fit for the results at 400 °C for 500 μN as well as for 1000 μN at 25 °C associated with the validation in Fig. 7.

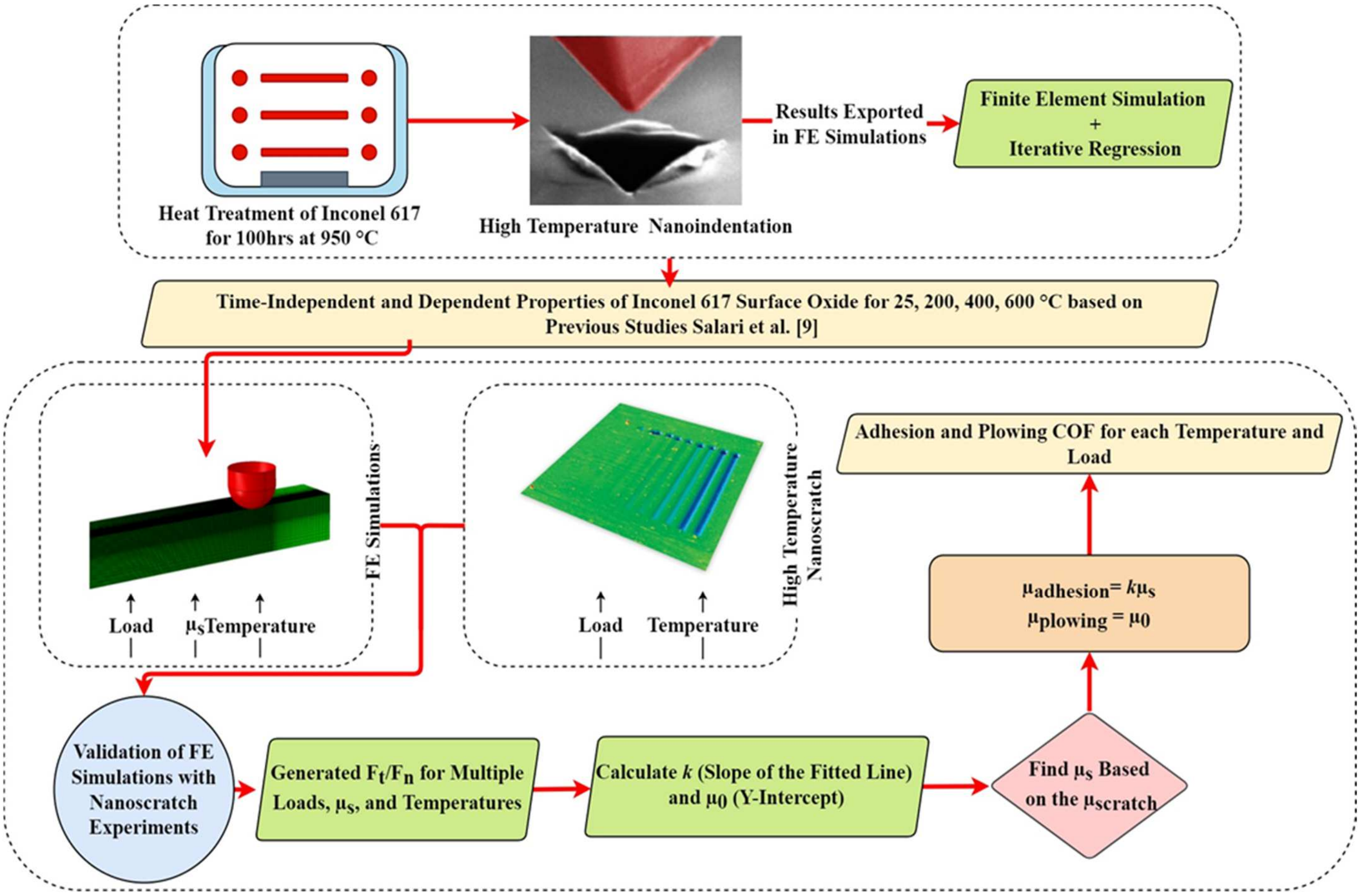

Fig. 5 Flow-chart of the process of extracting adhesion and plowing COF.

2.3. Numerical Modeling

An explicit solver was utilized within ABAQUS® 2020 to develop a three-dimensional replication of the scratch process, which contains a deformable cuboid in contact with a rigid indenter with a conospherical shape following the tip geometry used in the nanoscratch experiments (**Fig. 3**). The inputs for the material properties of the oxide (deformable cuboid) were obtained from the previous study exclusively performed on aged IN617 at temperatures up to 600°C [9]. The plastic deformation implemented in the FE simulations was based on the power-law strain hardening relation [9,26,27]:

$$\sigma_f = \sigma_y(1 + \frac{E_s \times \varepsilon_p}{\sigma_y})^{n_1} \quad (1)$$

where σ_f is the flow stress, n_1 represents the strain hardening exponent, E_s is the elastic modulus of the oxide and σ_y and ε_p denote the yield strength and plastic strain, respectively.

Three steps of indenting, scratching, and unloading were simulated similar to the experiments. During scratch step, once tangential load (F_t) stabilized, F_t over normal load (F_n) was utilized to calculate the total COF at several temperatures and loads (e.g., see **Fig. 4a** for F_t/F_n variation over time for 500 μN load at several temperatures). Once load was removed after the scratch step, residual scratch depth was recorded.

The COF evolution with temperature depends on the material and contact properties, crystallinity, and adhesion of the samples [28,29], however, it is often challenging to analyze COF at HTs. Here, FE simulations were used to determine the adhesion and plowing COF components as well as their evolution with temperature. Subhash and Zhang introduced an analytical model for the overall COF, μ, and its relation with the interfacial COF, μ_s, adhesion friction, μ_a and plowing friction, μ_p [17]. The linear relationship between the components can be written as [17]:

$$\mu = k\mu_s + \mu_0 \quad (2)$$

where k is the proportionality factor between the adhesion COF and interfacial COF, i.e., $\mu_a = k\mu_s$. It was assumed that the plowing term of total COF is independent of μ_s, and as a result one can assume $\mu_p = \mu_0$ [17]. That is, a linear relationship between constituents were assumed where k is the slope of the line and $\mu_p = \mu_0$ is the vertical axis intersection. For conical and Berkovich tips, earlier studies showed a linear relation between interfacial COF and overall COF [17–19]. However, it should be noted that one cannot generalize the linear relationship for all indenter types since it may be affected by the shape of the indenter.

For sliding simulations, one needs to apply nodal COF in the FE simulation. Following the work of Chamani and Ayatollahi, here, interfacial COF (μ_s) was considered to be an input variable for the FE model [19]. Considering ABAQUS FE software, μ_s is the input parameter that determines the COF

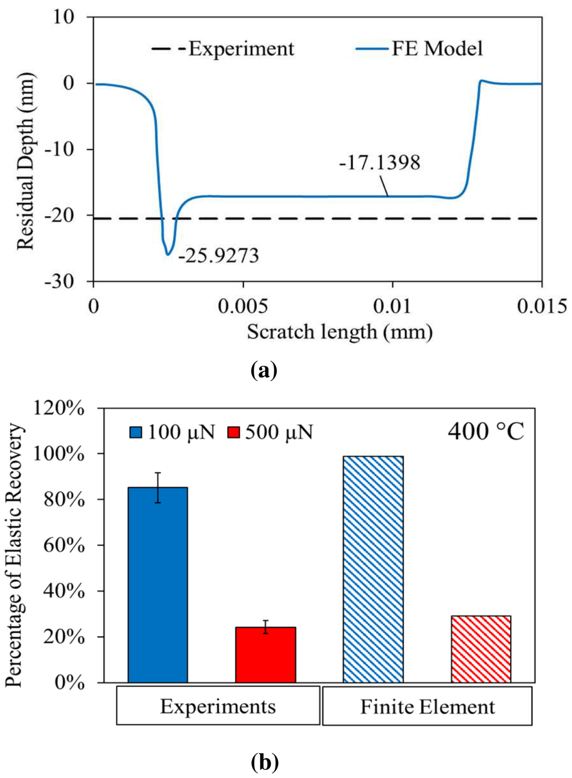

Fig. 6 Validation of the FE model against a) nanoscratch residual depth experiment data under normal load of 5 mN at room temperature and b) percentage of elastic recovery at 400 °C.

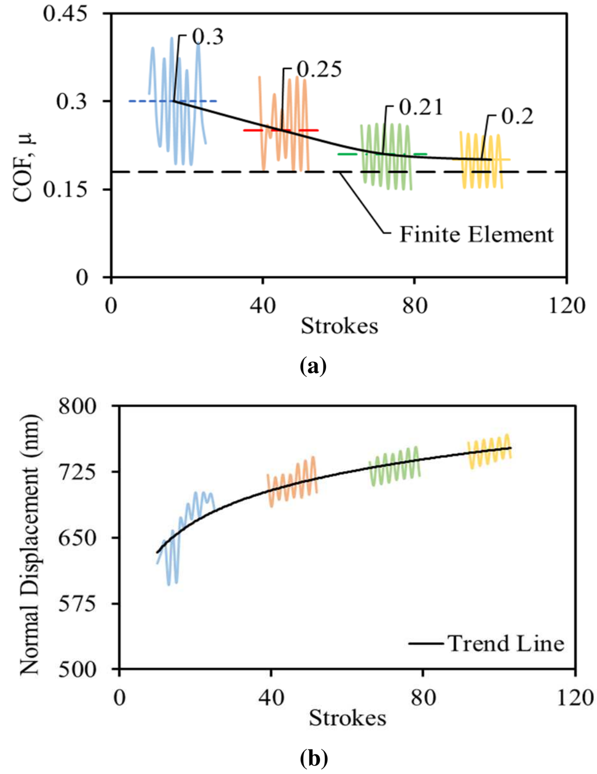

Fig. 7 a) Variation of COF and b) normal displacement with scratch passes, confirming the validity of the FE simulations under 1000 μN normal load.

between each node of the deformable sample with the rigid indenter based on Coulomb's law [18]. Interfacial COF (as an input of the simulation) was increased from zero to approximately 0.25 (also see Fig. 5) and the total COF was recorded. This, in fact, established the relation between total COF and the interfacial COF. As expected, for all conditions, linear behavior similar to Eqn. 2 was observed. The best linear fit for the results was then obtained to find the Y-intersection (vertical intersection), or the plowing component (μ_0) and the slope of the fit k (see **Fig. 4b** for the load of 500 μN). Finally, for each given condition, the associated experimental result (total COF) was used to find its interaction with the linear-fitted line which gives the X-interaction or μ_s and consequently μ_a. For instance, at 400°C and 500 μN load, an experimental μ value of ~0.17 was measured through scratch tests and was utilized to extract the components in Eqn. 2. In addition, energy dissipation during scratch process was recorded. ABAQUS calculates frictional energy based on the dissipated energy by the contact nodal friction forces. This energy is a direct function of interfacial COF and hence is considered as the adhesion energy. The software also estimates the plastic deformation energy throughout the process, and accordingly, this is considered as the plowing energy [30]. The overview of the current methodology is presented in **Fig. 5**.

3. Results and Discussion

To evaluate the robustness of the FE model, it is validated against multiple outputs of the experiments at different loads and temperatures. Residual depth versus scratch length of the FE model is shown in **Fig. 6a** along with the experimental scratch result at the load of 5 mN and 25 °C. Also, percentages of elastic recovery (η) measured through both experiments and simulations are depicted in **Fig. 6b** for loads of 100 μN and 500 μN at 400 °C. The degree of elastic recovery in the scratch process is defined in percentage as:

$$\eta = \frac{h - h_f}{h} \times 100 \tag{3}$$

where h denotes the in-situ scratch depth, and h_f is the residual depth.

It should be added that the final depth values at low temperatures are in sub-nm range and are in fact within the error of the FE simulations and, hence, cannot be utilized for verification. As seen, simulations show comparatively close results as compared to their associated experiments showing the validity of the FE model to simulate scratch for IN617.

A further validation step was taken to examine the validity of the overall methodology to capture components of the COF. Generally, two experimental methods exist to measure the adhesion component, single-pass, and multi-pass scratch tests [31]. In the former method, an indenter under low normal pressure slides over the surface while preventing considerable plastic deformation of the material [31]. In the latter, to

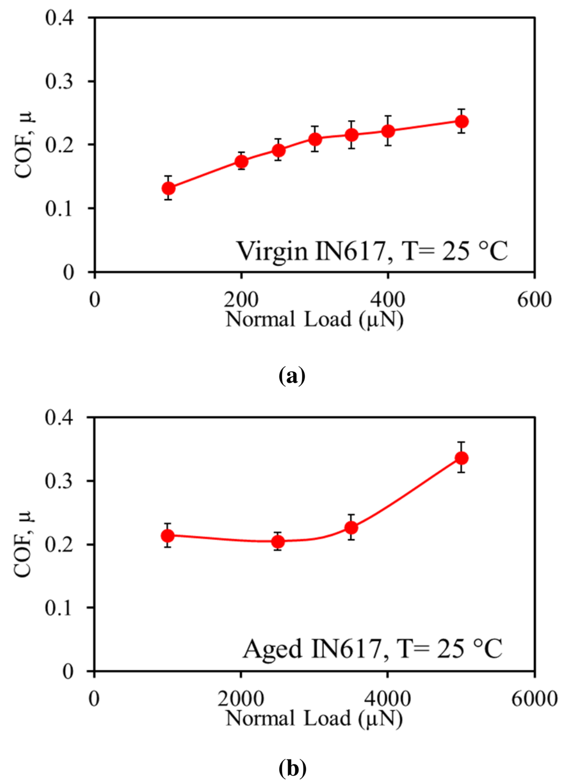

Fig. 8 Variation of COF with load for a) virgin sample and b) aged sample obtain through nanoscratch experiments

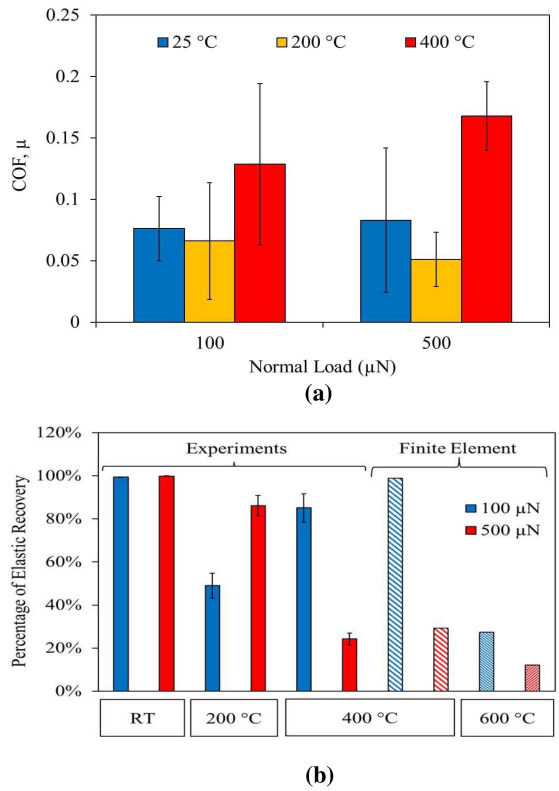

Fig. 9 a) Variation of COF with normal load and temperature measured through nanoscratch experiments and b) percentage of elastic recovery at different temperatures for loads of 100 μN and 500 μN on aged Inconel 617.

eliminate the effect of plowing, repeated reciprocating nanoscratches are performed and with each additional pass the plowing effect is reduced and is considered zero on the final cycle. Thus the final scratch gives the adhesive COF, μ_a [31]. Here, the second method was adopted utilizing a normal load of 1000 μN and a multi-pass reciprocating nanoscratch test. **Fig. 7a** shows the evolution of the COF during a multi-pass scratch test where each stroke represents a single one direction scratch. The oscillation in the COF is due to the reciprocating nature of the contact and the difference in COF values during forward and backward passes. To better evaluate the COF evolution, the average COF for 18 consecutive strokes were calculated at four different segments of the graph and are shown in **Fig. 7a.** It is evident that as the number of strokes increases, the COF reduces approaching a plateau (see also the trend line). At this stage, it is assumed that the measured COF is independent of the plowing component and can be considered to be the adhesion component of COF. **Fig. 7b** shows the associated normal displacement in the multi-pass scratch test. As seen, aligned with the COF values, displacement (due to plowing contribution of the COF) reaches a plateau with more passes. The first stroke (single scratch) of the above experiment was modeled using FE simulation and consequently the current methodology was utilized to extract the adhesion component. To further illustrate this case, the methodology and the linear fit used for the normal load of 1000 μN is also shown in **Fig. 4b**. As seen in **Fig. 7a**, the adhesion part of the COF derived from the combination of experiment and simulation is close to the final cycle experimental measures for IN617 surface oxide (within 10% error) confirming the validity of the methodology.

Fig. 8 shows the variation of experimental COF with normal load at a sliding velocity of 0.3 μm/s for both as-received (virgin) and aged samples. It can be observed that by increasing the load by 5-fold, the COF of both the virgin and aged samples increases significantly. This increase is more (91% increase) for virgin samples in comparison to aged IN617 (66% increase), which can be attributed to the difference in their yield strength. At room temperature, the yield strength of the oxide on top of IN617 (10.28 GPa) is much higher than that of the bulk (322 MPa) [9], hence the aged sample deformation is less sensitive to load increase and thus plowing parts of COF in aged sample does not change at the same rate as virgin samples.

Fig. 9a shows the experimental COF evolution of the aged IN617 oxide at different temperatures for two normal loads. Interestingly, and contrary to what is often observed at the macro level, the total COF increases with increasing temperature to 400 °C. The IN617 oxide is very hard at room temperature and 200 °C, hence, COF is less sensitive to load increase (deformation) as also seen in relatively constant COFs at 100 μN and 500 μN loads. However, previous measurements on the oxide of IN617 revealed that by increasing the temperature from room temperature to 400 °C, yield strength drops 70% [9]. Once oxide becomes softer, normal displacement and hence area under shear increases significantly and the contribution of plowing part of COF increases. At this condition, the COF is more sensitive to load as seen in **Fig. 9a** where COF increase 42 % at 400 °C by

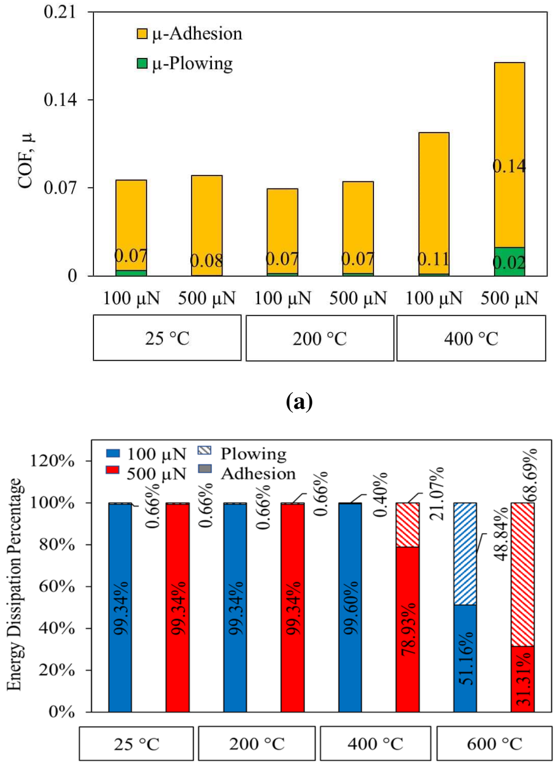

(b)

Fig. 10 a) Variation of COF and its constituents with normal load and temperature and b) energy dissipation due to friction at varied temperatures and loads extracted using the FE simulations. Solid colours show the adhesion contribution while patterned colours show the plowing contribution.

increasing the normal load from 100 µN to 500 µN. The effect of drop in yield strength can also be seen in elastic percentage recovery (η) depicted in **Fig. 9b.** It can be seen that with increasing load and especially increasing temperature, elastic recovery decreases. At a higher load of 500 µN in comparison to 100 µN, the influence of plastic deformation is more significant resulting in the reduction of η. Its effect is noticeable at 400 °C in which the elastic recovery declines significantly in comparison to RT. There exists also an apparent drop at 200 °C and 100 µN which is not consistent with the overall trend. Based on the current data, we cannot comment on the reason behind this, and further investigation is needed. Nevertheless, it should be noted that to assure the outcomes are correct, we repeated these tests several times and observed this consistently. FE simulations are also shown at 400 °C to confirm the model accuracy. The FE model makes it possible for the methodology to be extended to other temperatures, materials and geometries. Accordingly, here, the model was further utilized to extend the elastic recovery results for 600 °C which shows similar behavior to 400 °C. Yet at 600 °C, the difference between the two loads reduced, in comparison to lower temperatures probably due to already very high plastic deformation.

Fig. 10a shows the adhesion and plowing components of the COF, extracted based on the methodology discussed and with the help of FE simulations. For the selected loading conditions, while the overall COF increases with temperature and load, the plowing component becomes more dominant, especially at 400 °C confirming the observations in **Fig. 9**. While the adhesion part of COF is relatively constant at low temperatures and both loads, it increases by 120% to 200% at 400 °C for 100 µN and 500 µN, respectively. These results are also aligned with the FE results of energy dissipation due to friction for the two loads and varying temperatures (**Fig. 10b**). Aside from temperatures below 200 °C at which displacements are in nanometers, and, hence hard to be investigated by FE analysis, plowing energy dissipation is higher with temperature and force. In fact, similar behavior has been reported for nanoscratch results of an optical glass material [32].

4. Conclusion

For simplicity, the COF was broken to two concurrently occurring components: plowing and adhesion and was investigated through combined nanoscratch experiments and FE simulations. Elevated temperature nanoscratch was performed on the cross section of the oxide of aged samples and surface of virgin IN617. FE results were used to establish the relation between interfacial COF, reaction forces and find the components of the total COF. The main findings from this study are:

- Experimental results show no dependence of the COF on sliding velocity.
- Elastic recovery decreases with increasing load and temperature.
- The contribution of adhesion part of COF significantly increases with temperature.
- The effect of load and its concomitant plowing is only noticeable at 400 °C and 600°C, where the yield strength of oxide is lower than the RT and hence oxide deformation is considerable.
- The methodology presented herein can be extended to other geometries, temperatures, and materials.

Acknowledgement

We acknowledge the support from the U.S. Department of Energy (DOE) under NEUP Project 16-10732 as well as partial funding by George Mason University. Use of the Texas A&M University Materials Characterization Facility and Office of Research Computing (ORC) team support at George Mason University is also acknowledged.

References

[1] C. Cabet, A. Terlain, P. Lett, L. Guetaz, J. Gentzbittel, High temperature corrosion of structural materials under gas-cooled reactor helium, Mater. Corros. 57 (2006) 147–153.

[2] R.N. Wright, Kinetics of gas reactions and environmental degradation in NGNP helium, Citeseer, 2006.

[3] R.N. Wright, Summary of studies of aging and environmental effects on Inconel 617 and Haynes 230, 2006.

[4] M.S. Rahman, J. Ding, A. Beheshti, X. Zhang, A.A. Polycarpou, Elevated temperature tribology of Ni alloys under helium environment for nuclear reactor applications, Tribol. Int. 123 (2018) 372–384.

[5] M.S. Rahman, J. Ding, A. Beheshti, X. Zhang, A.A. Polycarpou, Helium Tribology of Inconel 617 at Elevated Temperatures up to 950° C: Parametric Study, Nucl. Sci. Eng. (2019) 1–15.

[6] A. Ahmadi, F. Sadeghi, S. Shaffer, In-Situ Friction and Fretting Wear Measurements of Inconel 617 at Elevated Temperatures, Wear. 410–411 (2018) 110–118. https://doi.org/10.1016/J.WEAR.2018.06.007.

[7] Y. Zheng, M.S. Rahman, A.A. Polycarpou, Self-welding of Inconel 617 under high-pressure-high-temperature conditions for nuclear reactors, Nucl. Eng. Des. (2020) 110941.

[8] V. Pauly, C. Tesch, J. Kern, M. Clark, D. Grierson, D. Singh, O. Ajayi, K. Sridharan, High-temperature tribological behavior of structural materials after conditioning in impure-helium environments for high-temperature gas-cooled reactor applications, J. Nucl. Mater. 522 (2019) 311–323. https://doi.org/10.1016/J.JNUCMAT.2019.05.025.

[9] S. Salari, M.S. Rahman, A.A. Polycarpou, A. Beheshti, Elevated temperature mechanical properties of Inconel 617 surface oxide using nanoindentation, Mater. Sci. Eng. A. 788 (2020) 139539. https://doi.org/10.1016/j.msea.2020.139539.

[10] F.P. Bowden, D. Tabor, Friction and Lubrication, Methuen & Co, Ltd. London. (1967).

[11] S. Lafaye, C. Gauthier, R. Schirrer, Analysis of the apparent friction of polymeric surfaces, J. Mater. Sci. 41 (2006) 6441–6452.

[12] J. Goddard, H. Wilman, A theory of friction and wear during the abrasion of metals, Wear. 5 (1962) 114–135.

[13] T. Palma, M. Munther, P. Damasus, S. Salari, A. Beheshti, K. Davami, Multiscale mechanical and tribological characterizations of additively manufactured polyamide 12 parts with different print orientations, J. Manuf. Process. 40 (2019) 76–83.

[14] M. Humood, A. Beheshti, A.A. Polycarpou, Surface reliability of annealed and tempered solar protective glasses: Indentation and scratch behavior, Sol. Energy. 142 (2017) 13–25. https://doi.org/10.1016/j.solener.2016.12.011.

[15] J. Valli, U. Mäkelä, A. Matthews, V. Murawa, TiN coating adhesion studies using the scratch test method, J. Vac. Sci. Technol. A Vacuum, Surfaces, Film. 3 (1985) 2411–2414.

[16] A. Grill, Review of the tribology of diamond-like carbon, Wear. 168 (1993) 143–153.

[17] G. Subhash, W. Zhang, Investigation of the overall friction coefficient in single-pass scratch test, Wear. 252 (2002) 123–134.

[18] H.R. Chamani, M.R. Ayatollahi, The effect of Berkovich tip orientations on friction coefficient in nanoscratch testing of metals, Tribol. Int. 103 (2016) 25–36.

[19] H.R. Chamani, M.R. Ayatollahi, Prediction of friction coefficients in nanoscratch testing of metals based on material flow lines, Theor. Appl. Fract. Mech. 94 (2018) 186–196.

[20] A. Chatterjee, A.A. Polycarpou, J.R. Abelson, P. Bellon, Nanoscratch study of hard HfB2 thin films using experimental and finite element techniques, Wear. 268 (2010) 677–685.

[21] A. Chatterjee, A. Beheshti, A.A. Polycarpou, P. Bellon, Yield maps for single and bilayer thin films under scratch, J. Tribol. 138 (2016).

[22] S.Z. Chavoshi, S.C. Gallo, H. Dong, X. Luo, High temperature nanoscratching of single crystal silicon under reduced oxygen condition, Mater. Sci. Eng. A. 684 (2017) 385–393. https://doi.org/10.1016/J.MSEA.2016.11.097.

[23] S.Z. Chavoshi, S. Xu, A review on micro-and nanoscratching/tribology at high temperatures: instrumentation and experimentation, J. Mater. Eng. Perform. 27 (2018) 3844–3858.

[24] J. Pujante, M. Vilaseca, D. Casellas, M.D. Riera, High temperature scratch testing of hard PVD coatings deposited on surface treated tool steel., Surf. Coatings Technol. 254 (2014) 352–357. https://doi.org/10.1016/J.SURFCOAT.2014.06.040.

[25] M. Varga, S. Leroch, H. Rojacz, M.R. Ripoll, Study of wear mechanisms at high temperature scratch testing, Wear. 388–389 (2017) 112–118. https://doi.org/10.1016/J.WEAR.2017.04.027.

[26] J. Kang, A.A. Becker, W. Sun, Determination of elastic and viscoplastic material properties obtained from indentation tests using a combined finite element analysis and optimization approach, Proc. Inst. Mech. Eng. Part L J. Mater. Des. Appl. 229 (2015) 175–188.

[27] E. Martínez-Pañeda, C.F. Niordson, On fracture in finite strain gradient plasticity, Int. J. Plast. 80 (2016) 154–167. https://doi.org/10.1016/J.IJPLAS.2015.09.009.

[28] T. Junge, J.F. Molinari, Plastic activity in nanoscratch molecular dynamics simulations of pure aluminium, Int. J. Plast. 53 (2014) 90–106. https://doi.org/10.1016/j.ijplas.2013.07.005.

[29] D.Q. Doan, T.H. Fang, T.H. Chen, Influences of grain size and temperature on tribological characteristics of CuAlNi alloys under nanoindentation and nanoscratch, Int. J. Mech. Sci. 185 (2020) 105865. https://doi.org/10.1016/j.ijmecsci.2020.105865.

[30] M. Smith, ABAQUS/Standard User's Manual, Version 2017, Simulia, 2017.

[31] S.C. Bellemare, M. Dao, S. Suresh, Effects of mechanical properties and surface friction on elasto-plastic sliding contact, Mech. Mater. 40 (2008) 206–219. https://doi.org/10.1016/j.mechmat.2007.07.006.

[32] C. Li, F. Zhang, Y. Ding, L. Liu, Surface deformation and friction characteristic of nano scratch at ductile-removal regime for optical glass BK7, Appl. Opt. 55 (2016) 6547. https://doi.org/10.1364/ao.55.006547.